applied sciences

MDPI

Article

Prediction of Fading for Painted Cultural Relics Using the Optimized Gray Wolf Optimization-Long Short-Term Memory Model

Zhen Liu [1], An-Ran Zhao [2,*] and Si-Lu Liu [2,*]

[1] College of Media, Qufu Normal University, Rizhao 276826, China; zhen@whu.edu.cn
[2] College of Engineering, Qufu Normal University, Rizhao 276826, China
* Correspondence: anran_z8377@163.com (A.-R.Z.); lsl_lsx@qfnu.edu.cn (S.-L.L.)

Abstract: Cultural heritage digitization is of great significance for the protection, restoration, and rejuvenation of cultural relics. In particular, the investigation of fading mechanisms is essential for virtual restoration to accurately recreate the original appearance of artifacts and facilitate humanistic and historical research. For the purpose of investigating the color fading mechanism of pigments, we propose a color fading time series model using a combined long short-term memory recurrent neural network modified by the gray wolf optimization algorithm (GWOAD-LSTM). First, the general gray wolf algorithm was scaled up to two dimensions and combined with an LSTM model for optimal parameter search. Second, six pigments commonly used in painted artifacts were subjected to simulated aging experiments. Third, by applying the experimental data to different predictors, the results of the Back Propagation Neural Network (BPNN), Long Short-Term Memory (LSTM), Long Short-Term Memory on Gray Wolf Optimizer (GWO-LSTM), and GWOAD-LSTM models were compared. The results showed that our proposed GWOAD-LSTM model outperformed other models in terms of accuracy and generalization ability, especially in predicting hLC color attributes. Our study aimed to provide a new application tool for the restoration and rejuvenation of painted artifacts.

Keywords: GWOAD-LSTM; pigment fading; hLC color attribute; prediction accuracy

check for updates

Citation: Liu, Z.; Zhao, A.-R.; Liu, S.-L. Prediction of Fading for Painted Cultural Relics Using the Optimized Gray Wolf Optimization-Long Short-Term Memory Model. *Appl. Sci.* **2024**, *14*, 9735. https://doi.org/10.3390/app14219735

Academic Editor: Pedro Couto

Received: 23 September 2024
Revised: 19 October 2024
Accepted: 22 October 2024
Published: 24 October 2024

Copyright: © 2024 by the authors. Licensee MDPI, Basel, Switzerland. This article is an open access article distributed under the terms and conditions of the Creative Commons Attribution (CC BY) license (https://creativecommons.org/licenses/by/4.0/).

1. Introduction

Painted cultural relics are treasures of Chinese classical culture. Currently, the construction of museums specializing in the preservation of historical and artistic works is growing, with an average annual growth rate of 7.7%. There are more than 4400 museums now. The number of excavated painted cultural relics has exceeded 900,000 items, including colorful architectural paintings, pottery paintings, and mural paintings [1]. These painted cultural relics reflect the exceptional craftsmanship of ancient China. They are not only the embodiment of human wisdom but also significant symbols of historical progress, possessing historical, artistic, and scientific value. However, the painted pigments of excavated cultural relics are subject to aging, inadequate protection measures, and other external influences, causing faded color and blurry patterns. The damage rate has reached an alarming extent of 50.66% [2]. Numerous factors, such as light exposure, humidity, temperature, microbial degradation, and air quality, cause permanent damage to painted cultural relics; this damage is mainly manifested as fading, discoloration, peeling, and powdering, as illustrated in Figure 1. These issues have severely affected the artistic and archeological value of relics.

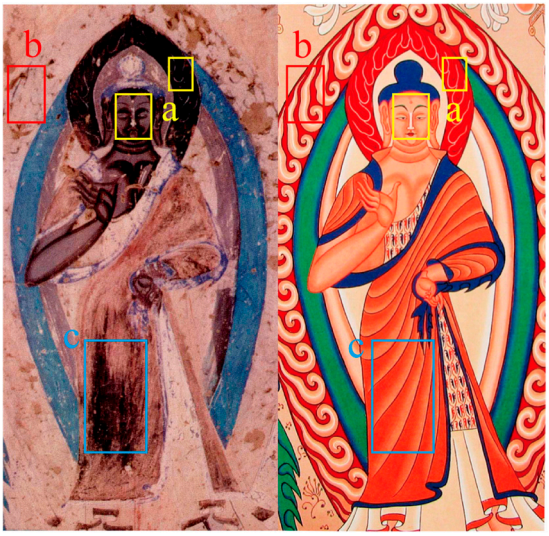

Figure 1. Comparison of the copy restoration of Cave 249 (Western Wei dynasty) of the Mogao Caves (yellow box "a" is fading color; red box "b" is peeling skin; blue box "c" is de-powdering).

The restoration of faded colors in cultural relics is crucial for the study of historical culture, as valuable information about the production, life, beliefs, and artistic level of ancient civilizations may be contained in painted cultural relics. Restoring the faded color of cultural relics can reveal their historical color and appearance, providing more accurate information for the study of historical culture. In the process of restoring faded colors, it is essential to respect the historical and original characteristics of the artifacts and to avoid any arbitrary changes or additions that may cause irreversible damage. Therefore, the study of the optical, chemical, and temporal characteristics of pigments and the development of virtual restoration techniques to understand the mechanisms of chronological fading are essential for the digital preservation of cultural relics.

In recent years, domestic and international scholars have conducted a large amount of research on the conservation of painted cultural relics and other related issues. For example, researchers at the Munsell Laboratory in the United States, led by Berns [3], have utilized the Kubelka–Munk theory to identify the primary fading pigment as rouge. They conducted virtual restoration of the color in specific areas of Vincent Van Gogh's painting "Bedroom." Hyperspectral imaging and scanning XRF spectrometry were utilized by Kirchner [4,5] from the Netherlands to determine the spatial distribution of the pigments in Van Gogh's "Field with Irises near Arles," and then the Kubelka–Munk model was used to determine a concentration map for all pigments to achieve a virtual recovery of this painting. The color change mechanism of lead white pigment in mural paintings was investigated by Bruder et al. [6] by utilizing laser-induced breakdown spectroscopy. They found that lead and oxygen elements formed lead oxides, which surrounded the surface of the pigment particles, inducing a change in color appearance. The impact of pigment fading on painted cultural relics was discussed, and the threshold at which discoloration occurred was estimated. Tang [7] and Li [8], along with other researchers, conducted a series of long-term pigment aging simulation experiments and made several notable findings that lead-based pigments were easier to discolor under prolonged exposure to ultraviolet light, ozone, carbon dioxide, or hydrogen sulfide. Higher humidity levels were observed to have a more significant impact on the fading degree of lead yellow and lead red pigments under ultraviolet light. In the case of cinnabar and earth red pigments, prolonged exposure to sunlight was not the main factor causing discoloration. Notably, the degradation of the organic binders was the main cause. Sheng et al. [9] found that lead red pigments that were not mixed with organic binder faded more readily under UV fluorescence irradiation at 90% humidity than lead red pigments that were mixed with organic binder. The protective and inhibitory effects of organic binder on pigment

discoloration were discussed. Gong et al. [10] investigated the effect of humidity and organic binders on the fading of lead red pigments. They observed that the fading rate of binder-free lead red was faster than that of lead red pigments mixed with binders when the time of exposure to UV was extended. Furthermore, a higher humidity level resulted in faster initial fading rates, but fading in the later stages was not noticeable. Zhao et al. [11] simulated the irradiation of painted cultural relics by ten narrow-band spectra. The adverse impact data of different spectra on color for various types of pigments were collected, analyzed, and fitted to develop damage functions. These damage functions could serve as a basis for light source selection and access standard determination in the lighting of painted relics. The research mentioned above has achieved some results on the virtual restoration of painted relics and the determination of fading factors of pigments. However, there is a gap in the research of the chronological fading mechanism.

Investigating the chronological mechanisms of pigment fading can provide valuable insights for the restoration of painted cultural artifacts. In the field of artificial intelligence, the long short-term memory (LSTM) network architecture was proposed by Hochreiter and Schmidhuber [12] in 1997. This architecture effectively addressed issues such as exploding gradients and vanishing gradients, which were commonly encountered in recurrent neural networks. Superior performance in short-term prediction tasks was demonstrated by the LSTM model compared to conventional prediction models. However, the LSTM model involved intricate hyperparameters that were not explicitly defined. Hyperparameters are predetermined values that are set before the start of machine learning. Different choices of hyperparameters result in different expected outcomes. Therefore, the rational selection of hyperparameters became a vital and challenging aspect of simulating time series prediction in machine learning. To tackle the aforementioned challenges, Mirjalili [13] proposed the gray wolf optimizer (GWO) in 2014, an optimization algorithm inspired by the social behavior of gray wolves. Rapid convergence and global search optimization were demonstrated by this algorithm. The hyperparameter selection problem was effectively addressed by iteratively optimizing the hyperparameter values. Furthermore, Pan et al. [14] introduced the GWO-LSTM composite model, which outperformed the standalone LSTM model in terms of chronological regression, prediction accuracy, and generalization capability. In recent years, scholars have made further advancements to enhance the model's performance. For example, Luo et al. [15] proposed an enhanced GWO algorithm based on complex-valued encoding, representing the genes of gray wolves as diploids, significantly expanding the information content of individual genes. The exploration and exploitation abilities of the GWO were balanced by Long et al. [16] through the adjustment of parameter "a" to prevent the model from becoming trapped in local optima. Improved algorithms, such as those mentioned above, followed the "No Free Lunch Theorems for Optimization", where any enhanced performance over one class of problems was offset by the performance over another class of problems [17]. Thus, these algorithms are not ideal for application in the fading of painted pigments of cultural relics.

In summary, domestic and international research on the mechanism of pigment fading has been limited to the stage of conducting simulated aging experiments. Certain drawbacks are possessed by them. For instance, it takes approximately 480 h of exposure for lead red to show noticeable fading. Aging experiments require a considerable amount of time and money. Traditional Chinese painting predominantly uses mineral pigments and a small amount of plant-based pigments, which is very different from Western painting practices. The application of artificial intelligence to the fading mechanism of pigments has not been proposed.

We combined the mechanism of pigment fading with time series analysis and proposed an improved optimization model, called the GWO for ascending dimensions (GWOAD). This model increased the dimensions of each gray wolf to extend the location information and improve the initial population diversity. The robustness and exploratory capability of the model were enhanced to optimize the hyperparameters of the LSTM model. This model also had the advantage of avoiding local optima. Finally, an improved gray wolf

optimization–long short-term memory (GWOAD-LSTM) composite prediction model was constructed and compared with the BPNN, LSTM and GWO-LSTM models. Aging experiments were conducted using six pigments: lead red, lithargite, rouge, cinnabar, azurite, and malachite. These were used investigate the effectiveness of the GWOAD-LSTM composite model in the optical aspect of deteriorated pigments and to provide technical references for predicting pigment fading, color restoration, and preservation of painted cultural artifacts. Furthermore, a correlation between the prediction accuracy errors of different categories of pigments and the appearance of pigment deterioration was established. The mechanism of influence of raw data on prediction accuracy was analyzed from the perspective of chromatics, optics, and chemistry.

2. Prediction Principles of the LSTM and GWOAD Models

2.1. Long Short-Term Memory (LSTM) Model Principles

LSTM is a type of recurrent neural network (RNN) with memory functionality that was proposed by Hochreiter and Schmidhuber in 1997. Compared to traditional RNNs, LSTM incorporates memory cells that allow for the discrimination of useful information [12]. As shown in Figure 2, LSTM consists of four "gates" for information processing: the forget gate f, input gate i, output gate o, and a memory cell c.

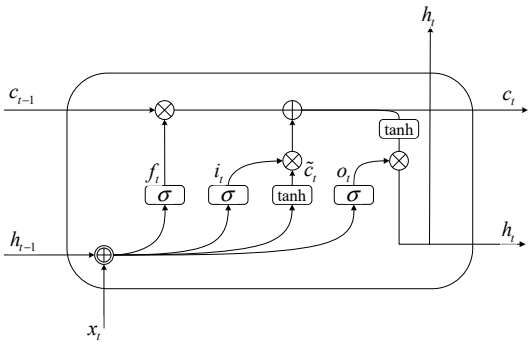

Figure 2. Structure of the LSTM network unit at time t.

The pigment time series data at a time t, as the input information matrix x_t, and the output signal matrix h_{t-1} at the previous time form the forget gate to select the cell state c_{t-1} at the previous time. Then, the forget gate matrix f_t is as follows:

$$f_t = \sigma\left(W_f x_t + U_f h_{t-1} + b_f\right) \tag{1}$$

where σ is the sigmoid function; W_f and U_f are the forget gate weight matrices; and b_f is the forget gate offset parameter matrix. Second, the input gate determines what information should be stored in the current state c_t; then, the following is obtained:

$$i_t = \sigma(W_i x_t + U_i h_{t-1} + b_i) \tag{2}$$

$$\widetilde{c}_t = tanh(W_c x_t + U_c h_{t-1} + b_c) \tag{3}$$

where i_t is the input gate matrix of the neuron at time t; $\widetilde{c}_t$ is the cell candidate state matrix of the neuron at time t; W_i and U_i are the input gate weight matrix; b_i is the input gate offset parameter matrix; W_c and U_c are the cell candidate state weight matrix; and b_c is the cell candidate state offset parameter matrix. From Equations (1)–(3), the unit state matrix c_t of the momentary neuron is as follows:

$$c_t = f_t \otimes c_{t-1} + i_t \otimes \widetilde{c}_t \tag{4}$$

where $\otimes$ is the dot product of the matrix. Finally, the output gate determines the output control of the cell state c_t to h_t at the current moment; then, the following is obtained:

$$o_t = \sigma(W_o x_t + U_o h_{t-1} + b_o) \tag{5}$$

$$h_t = o_t \otimes tanhc_t \tag{6}$$

where o_t is the output gate matrix of the neuron at time t; W_o and U_o are the output gate weight matrix; b_o is the output gate offset parameter matrix; and h_t is the output matrix of the neuron at time t.

The LSTM model selectively discards, retains, and controls the output values of the pigment data at the previous moment by introducing a cell state through the forget gates, input gates, output gates, and a memory cell. This approach helps to avoid overfitting and the delivery of interference information and alleviates the issues of exploding gradients and vanishing gradients encountered in traditional recurrent neural networks (RNNs). Furthermore, LSTM resolves the problem of the long-term dependency nature of RNNs, causing it to be suitable for short-term memory time series regression tasks.

2.2. Gray Wolf Optimization (GWO) Model Principles

The gray wolf optimization (GWO) algorithm is an optimal data processing intelligence algorithm proposed by Mirjalili et al. in 2014 and is based on simulating the hunting behavior of natural gray wolf populations. Information is accurately acquired by iteratively updating to approach the prey [13]. As shown in Figure 3, the leadership hierarchy of the gray wolf population can be divided into $\alpha, \beta, \delta, \omega$, with leadership power $\alpha > \beta > \delta > \omega$, which correspond to optimal, suboptimal, third-optimal, and other solutions, respectively. α, β, δ direct ω to continuously chase, drive, approach, and harass the prey, which causes them to stop moving and thus achieve a precise attack.

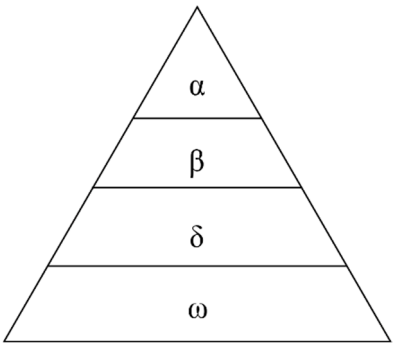

Figure 3. Wolf pack algorithm leadership hierarchy diagram.

As shown in Figure 4, during the encircling process led by the alpha wolf α, the gray wolf pack surrounds the prey. This process can be mathematically defined as follows:

$$\vec{D} = \left| \vec{C} \cdot \vec{X}_{P,k} - \vec{X}_k \right| \tag{7}$$

$$\vec{X}_{k+1} = \vec{X}_{P,k} - \vec{A} \cdot \vec{D} \tag{8}$$

where $\vec{D}$ represents the distance vector between an individual and the prey, k denotes the iteration number, and $\vec{X}_k$ and $\vec{X}_{P,k}$ represent the position vectors of the k-th gray wolf and the prey, respectively, in the k-th iteration. Specifically, Equation (8) describes the position

update formula for a gray wolf based on the new distance. The coefficients in Equation (8) are denoted as $\vec{A}$ and $\vec{D}$ vectors, and their formulas are as follows:

$$\vec{A} = 2\vec{a} \cdot \vec{r}_1 - \vec{a} \tag{9}$$

$$\vec{C} = 2\vec{r}_2 \tag{10}$$

where $\vec{a}$ is a convergence vector that gradually decreases linearly from 2 to 0 as the number of iterations increases; $\vec{r}_1$ and $\vec{r}_2$ are the random vectors whose elements are taken as [0, 1]; and $\vec{C}$ is the random number of [0, 2], indicating the weight coefficient occupied by the prey. After the wolf pack has completed the encircling process, with the wolves α, β, δ being the closest to the prey, the remaining wolves in the pack (represented by vector ω) start hunting and gradually approach the prey. By improving the traditional distance formula in Equations (7) and (8) to a distance formula with two positional attributes, the positional update formula for the wolves in wolf packs α, β, δ, and ω can be expressed as follows:

$$\begin{cases} \vec{D}_\alpha = \left| \vec{C}_1 \cdot \vec{X}_{\alpha,k} - \vec{X}_k \right| \\ \vec{D}_\beta = \left| \vec{C}_2 \cdot \vec{X}_{\beta,k} - \vec{X}_k \right| \\ \vec{D}_\delta = \left| \vec{C}_3 \cdot \vec{X}_{\delta,k} - \vec{X}_k \right| \end{cases} \tag{11}$$

$$\begin{cases} \vec{X}_{1,k+1} = \vec{X}_{\alpha,k} - \vec{A}_1 \cdot \vec{D} \\ \vec{X}_{2,k+1} = \vec{X}_{\beta,k} - \vec{A}_2 \cdot \vec{D} \\ \vec{X}_{3,k+1} = \vec{X}_{\delta,k} - \vec{A}_3 \cdot \vec{D} \end{cases} \tag{12}$$

$$\vec{X}_{\omega,k+1} = \frac{1}{3}\left(\vec{X}_{1,k+1} + \vec{X}_{2,k+1} + \vec{X}_{3,k+1} \right) \tag{13}$$

where $\vec{D}_\alpha, \vec{D}_\beta, \vec{D}_\delta$ are the distance vectors between α, β, δ and the prey, $\vec{X}_{\alpha,k}, \vec{X}_{\beta,k}, \vec{X}_{\delta,k}$ are the position vectors of the k-th iteration of α, β, δ, $\vec{X}_{1,k+1}, \vec{X}_{2,k+1}, \vec{X}_{3,k+1}$ are the position vectors of the $(k+1)$-th iteration between ω and α, β, δ, and $\vec{X}_{\omega,k+1}$ is the final position vector of the $(k+1)$-th iteration.

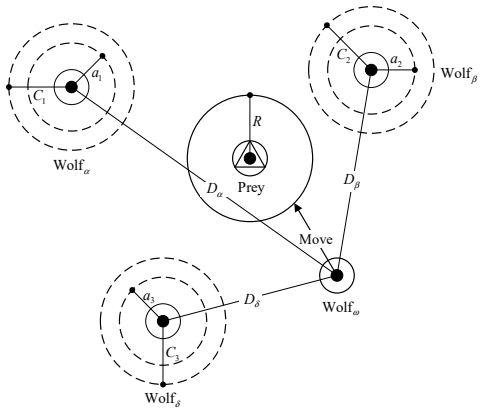

Figure 4. Schematic diagram of GWO algorithm gray wolves approaching prey.

Finally, as the gray wolves gradually approach the prey, the $\vec{a}$ vector linearly decreases from 2 to 0. The elements of vector $\vec{A}$ fluctuate within the range $[-a, a]$. When $|\vec{A}| < 1$, the prey has stopped moving, and the wolves pack attack the prey to achieve a global optimum

and optimize the parameter values. However, if $|\vec{A}| > 1$, the wolf pack starts searching for new optimal positions to avoid becoming trapped in local optima [18]. This process is illustrated in Figure 5.

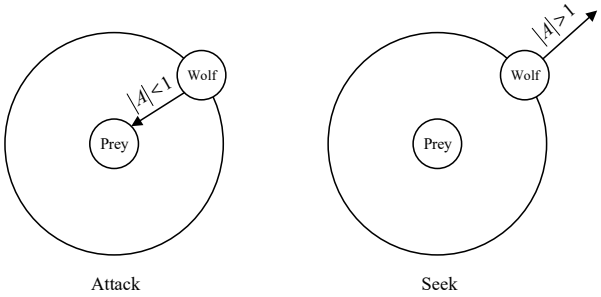

Figure 5. Schematic diagram of attacking prey and finding prey.

2.3. Gray Wolf Optimization for Ascending Dimension (GWOAD) Model

The GWO model has poor population diversity due to the random initial population, and the goodness of the initial population has a great impact on the global convergence speed and optimization quality of parameter search. The population diversity is closely related to the optimization ability of the algorithm, a larger number of wolves will reduce the global convergence speed; a smaller number of wolves will not achieve the optimization parameter quality. The main reason for this is the distance formula between gray wolves and prey in the traditional GWO model, because this formula is scalar, and the information covered in the formula is limited, and solving this problem requires increasing the number of gray wolves and the number of populations, which affects its convergence speed. In the traditional GWO model, the random definition of the initialized population does not guarantee optimal results.

Based on this, to address the problem of the influence of the number of gray wolves on the global convergence speed and the amount of parameter search quality, this paper improves the diversity of the initial population in the GWO model, and proposes that the GWOAD (GWO for Ascending Dimension) raises the parameters in the traditional gray wolf distance position to two dimensions, and each wolf in the plains in the east–west and the north–south direction (x and y) should be considered in two dimensions for position updating to simulate the hunting behavior of gray wolf packs in realistic environments:

$$R_1 = \begin{bmatrix} r_{1x} & \\ & r_{1y} \end{bmatrix} \tag{14}$$

$$R_2 = \begin{bmatrix} r_{2x} & \\ & r_{2y} \end{bmatrix} \tag{15}$$

where r_{ix} and r_{iy} represent random numbers between 0 and 1 for the x and y dimensions, respectively. $i = 1, 2$. Therefore, the modified forms of Equations (9) and (10) can be expressed as follows:

$$A = 2a'R_1 - a'E \tag{16}$$

$$C = 2R_2 \tag{17}$$

where R_1 and R_2 represent random diagonal matrices of size 2×2 with values ranging from 0 to 1 for the x and y dimensions, respectively, and E represents the identity matrix of size 2×2. To consider the fitness values of the wolf pack to prevent them from becoming trapped in local optima, the equations can be modified as follows:

$$a' = 2[1 - \sin(i/i_{max})\pi] \tag{18}$$

where i represents the current iteration number and i_{max} represents the maximum number of iterations. Therefore, a' nonlinearly decreases from 2 to 0 as the iteration progresses. The position of the predator wolves is updated to the following:

$$\begin{cases} D_\alpha = \left| C \times X_{\alpha,k} - X_k \right| \\ D_\beta = \left| C \times X_{\beta,k} - X_k \right| \\ D_\delta = \left| C \times X_{\delta,k} - X_k \right| \end{cases} \tag{19}$$

$$\begin{cases} X_{1,k+1} = X_{\alpha,k} - A \times D \\ X_{2,k+1} = X_{\beta,k} - A \times D \\ X_{3,k+1} = X_{\delta,k} - A \times D \end{cases} \tag{20}$$

where D_α,D_β,D_δ represents the 2×2 distance matrix between group α, β, δ and the prey, $X_{\alpha,k}$,$X_{\beta,k}$,$X_{\delta,k}$ represents the 2×2 position matrix of group α, β, δ in the k-th iteration, and $X_{1,k+1}$,$X_{2,k+1}$,$X_{3,k+1}$ represents the 2×2 position vector between group ω and group α, β, δ in the $(k+1)$-th iteration. There is a compromise on the two-dimensional information. Therefore, the position information of group ω in the x and y dimensions can be expressed as follows:

$$\begin{cases} \vec{X}_{\omega,k+1,x} = \frac{1}{3} sin(\theta) \left(\vec{X}_{1,k+1,x} + \vec{X}_{2,k+1,x} + \vec{X}_{3,k+1,x} \right) \\ \vec{X}_{\omega,k+1,y} = \frac{1}{3} cos(\theta) \left(\vec{X}_{1,k+1,y} + \vec{X}_{2,k+1,y} + \vec{X}_{3,k+1,y} \right) \end{cases} \tag{21}$$

where $\vec{X}_{\omega,k+1,x}$,$\vec{X}_{\omega,k+1,y}$ represents the position vector in the x and y dimensions, and θ represents a random number between 0 and $\pi/2$. Each gray wolf has its position information in the two-dimensional coordinate system. The final position of group ω is updated as follows:

$$\vec{X}_\omega = sgn(\vec{X}_{\omega,k+1,x} + \vec{X}_{\omega,k+1,y}) \sqrt{(\vec{X}_{\omega,k+1,x})^2 + (\vec{X}_{\omega,k+1,y})^2} \tag{22}$$

In the equation, "sgn" represents the sign function. The final position update for group ω incorporates the observed prey position information from group α, β, δ in both the x and y dimensions. By elevating the position information provided by regular gray wolves, the information is observed and independently updated in different dimensions. This greatly expands the amount of information contained within the individual gray wolf, enhances the diversity of the population, and improves the search performance of the gray wolves. Additionally, the information in these two dimensions strengthens the individual gray wolf and diversifies the variables of information of the population, thereby avoiding local optima. The schematic diagram is shown in Figure 6.

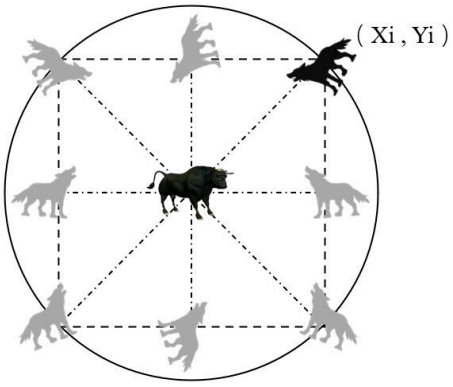

Figure 6. Schematic diagram of GWOAD in two dimensions.

2.4. GWOAD-LSTM Model

The LSTM model is processed by four special "gates" to achieve temporal prediction of the pigment fading data signal. However, the selection of hyperparameters in the LSTM network can affect the prediction results of the LSTM data. In terms of hyperparameter selection, the multidimensional characteristics of GWOAD was adopted to globally and automatically optimize the maximum hidden units, the maximum training cycle, and the initial learning rate in the LSTM network. This approach helped to avoid wasting time and resources in parameter tuning and prevent overfitting. The process is illustrated in Figure 7.

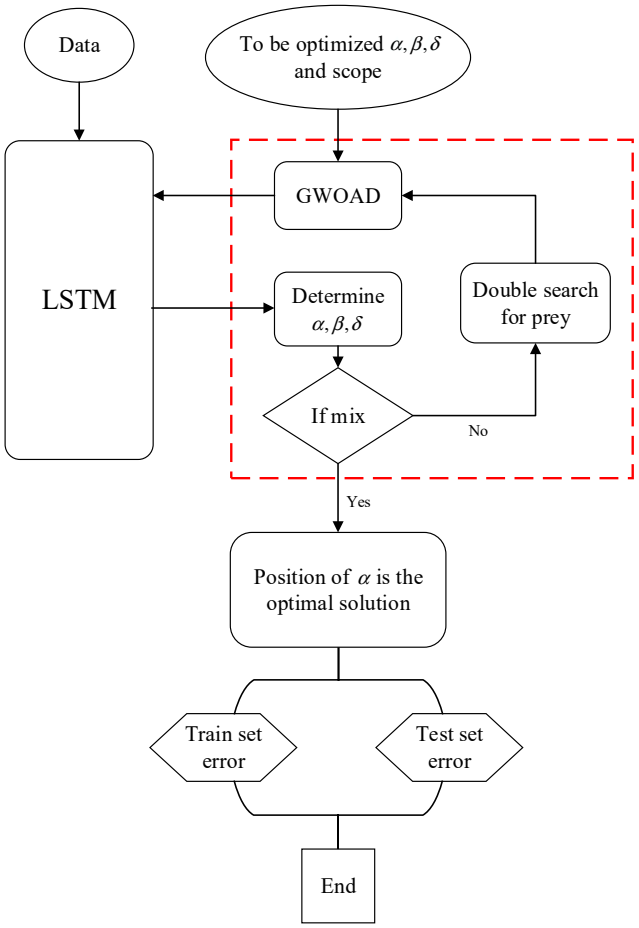

Figure 7. GWOAD-LSTM Workflow. (The red box shows the improved GWOAD parameter optimization process).

3. Experiment

3.1. Subsection Experimental Materials and Instruments

(1) Instruments: An X-rite Ci64 integrating sphere spectrophotometer was used with a wavelength range 400 nm to 700 nm and wavelength interval of 10 nm. A sunlight simulated light bulb (Model ULTRA VITALUX 300 W 230 V E27 (OSRAM PIA, Wilmington, MA, USA), radioactive power 280–315 nm (UVB) (Haorun Illumination Technology Co., Ltd., Foshan, Guangzhou, China), 315–400 nm (UVA) (Haorun Illumination Technology Co., Ltd., Foshan, Guangzhou, China)) was used. A modified simulation aging box was utilized.

(2) Materials: Tian Ya mineral pigments of lead red, lithargite, cinnabar, Stone Breen and malachite, and Chinese traditional light color painting plant pigment of rouge, gelatin, and ceramic tile were used.

3.2. Preparation of Fading Sample Color Cards

Following the research methods and techniques described in the relevant literature in recent years [19,20], the traditional Chinese mineral pigments, including lead red, lithargite, rouge, cinnabar, azurite, and malachite, were dispersed and blended with gelatin in specific proportions. The mixture was then applied to corresponding ceramic tiles using a paintbrush, ensuring an even dispersion of the pigments on the ceramic surface without any de-powdered or peeling phenomenon.

3.3. Simulation Aging of the Fading Sample

In this experiment, the optical simulation aging was conducted in a completely dark environment. The following steps were taken:

1. Setting the Simulated Aging Box: The aging box was adjusted to simulate environmental parameters similar to those of the Mogao Grottoes. Considering the significant temperature and humidity differences between day and night at the grottoes, the temperature and humidity in the aging box were adjusted accordingly.

2. External Isolation: A blackout curtain was used to isolate the aging box to prevent any external light variations from affecting the experiment.

3. Arrangement and Illumination of the Fading Samples: The fading samples were placed below the light source in a circular arrangement. The height distance between the light source and the samples was adjusted to ensure that each sample received the same irradiance on its surface. Moreover, the distribution of the spectrum of the light source was periodically tested and replaced to prevent any abnormal phenomena, such as light decay, from affecting the accuracy of the aging experiment. The light source spectral distribution curve of the aging samples and experimental equipment is shown in Figure 8.

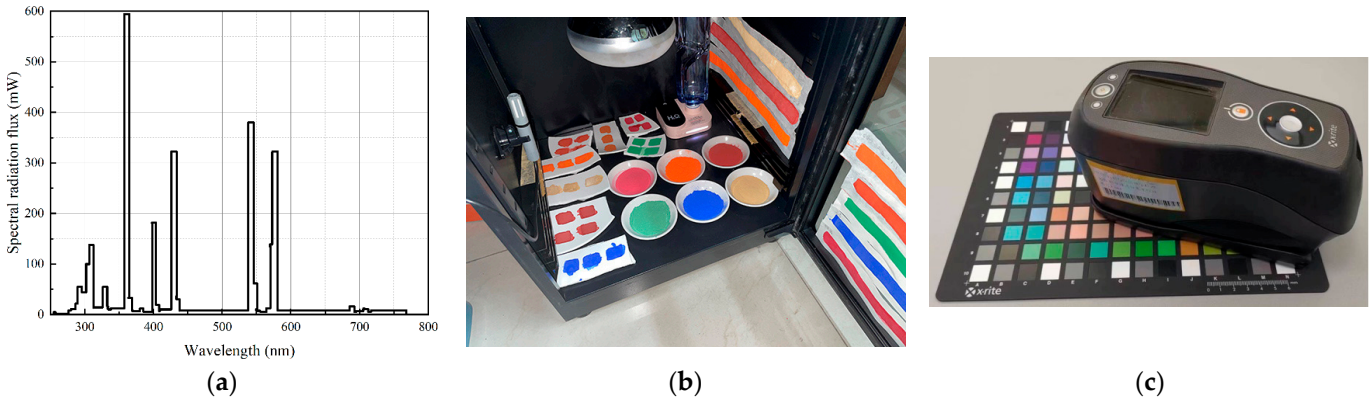

Figure 8. Spectral distribution curve of light source (**a**), and fading samples and experimental equipment display diagrams (**b**,**c**).

The total number of cycles in this experiment was 102, with 10 h per cycle, for a total irradiation duration of 1020 h. An X-rite Ci64 integrating sphere spectrophotometer (X-Rite, Grand Rapids, MI, USA) was used to measure the colorimetric properties of each fading sample in the range of 400 to 700 nm under a D50 light source, 2-degree viewing angle, D/8° illumination geometry, and a 6 mm aperture. The measurement data were organized accordingly. Subsequently, the GWOAD-LSTM composite model was used for time series regression analysis of the hLC (hue, lightness, and chroma) values of the fading samples as the exposure time increased. This analysis aimed to predict the corresponding hLC variations of the six fading sample cards caused by the simulated sunlight exposure.

After prolonged exposure to light, all six pigments exhibited uneven color patches on the surface. As shown in Figure 9, lead red and lithargite exhibited dark patches on their surfaces, particularly lithargite, which changed from its original bright yellow color to a deep brownish coffee color. Rouge showed the most severe damage, with partial cracking and significant fading. The cinnabar had a dark layer covering its entire surface. Azurite

had relatively minor changes, with a few white patches on the surface. Some areas of the malachite pigment transformed from white light green to dark green.

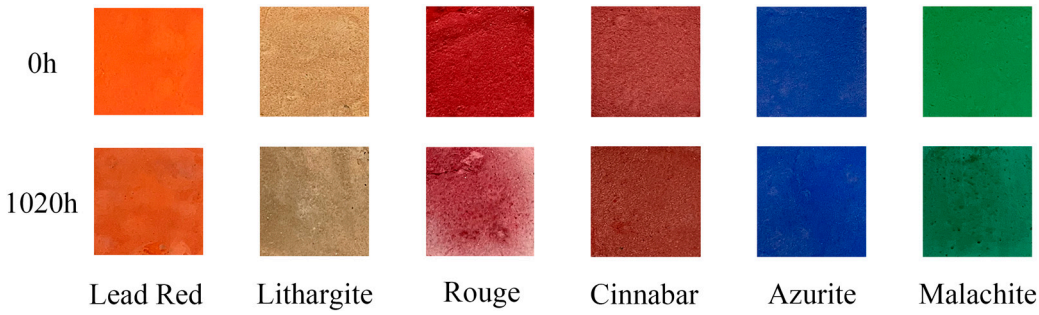

Figure 9. Comparison chart of six pigment diseases.

4. Results and Discussion

The MATLAB 2022a programming language was used to build the temporal prediction models of BPNN, LSTM, GWO-LSTM and GWOAD-LSTM, the number of predictions of each model was five times, which were averaged, and the prediction results were plotted. For each pigment, the root mean square error (*RMSE*), mean absolute error (*MAE*), and mean absolute percentage error (*MAPE*) were selected as the evaluation metrics. The error metrics of the four models when predicting these six pigments were used to evaluate the performance of the model. The effect mechanism of illumination on the color value was also analyzed. The expressions for each evaluation metric are as follows:

$$RMSE = \frac{1}{n}\sum_{i=1}^{n}|y_t - y_p| \tag{23}$$

$$MAE = \sqrt{\frac{1}{n}\sum_{k=1}^{n}(y_k - y'_k)^2} \tag{24}$$

$$MAPE = \frac{1}{n}\sum_{k=1}^{n}\left|\frac{y_k - y'_k}{y_k}\right| \times 100\% \tag{25}$$

where n is the number of samples; y_k is the predicted value; and y'_k is the true value; smaller *RMSE*, *MAE*, and *MAPE* values correlated with a better prediction of the model.

4.1. Determination of Model Parameters

In this study, the prediction step size was set to three, which meant that the reconstruction of the dataset was performed for the data points of the previous three cycles for each feature, and the fourth cycle value of the output feature was predicted to achieve regression prediction based on time features. Due to the small fluctuation range of the pigment model data and to distinguish the prediction accuracy of the different models, the number of input features was established as 11 (L, a, b, X, Y, Z, R, G, B, C, h), and the number of output features was 1 (consisting of hue h, lightness L, and chroma C). The number of nodes in the BPNN model's hidden layer was set to two, the max epoch was set to 100, the initial learning rate was set to 0.1, and the minimum error of the training objective was set to 0.01. The single LSTM model had 20 hidden units, a max epoch of 100, and an initial learning rate of 0.1. The determination of the specific parameters for the single LSTM model was based on empirical settings. Through experimental simulations, the number of gray wolves in the GWOAD and GWO algorithms was determined to be 15, with a max iteration of 10. The upper and lower boundaries were set as 15, 50, and 0.001 and 60, 450, and 0.1, respectively. The optimized parameters of the LSTM model are shown in Tables 1 and 2.

Table 1. Optimization parameters of GWO.

Pigment Type	Prediction Type	Number of Hidden Units	Number of Epochs	Initial Learning Rate
Lead Red	h	17	188	0.0993
	L	45	94	0.0499
	C	50	313	0.0144
Lithargite	h	25	201	0.0025
	L	44	250	0.0360
	C	22	174	0.0194
Rouge	h	38	155	0.0601
	L	46	265	0.0139
	C	26	160	0.0889
Cinnabar	h	18	131	0.0402
	L	16	52	0.0147
	C	35	202	0.0112
Azurite	h	20	257	0.0362
	L	18	308	0.0262
	C	17	272	0.0241
Malachite	h	19	329	0.0468
	L	23	203	0.0860
	C	35	296	0.0189

Table 2. Optimization parameters of GWOAD.

Pigment Type	Prediction Type	Number of Hidden Units	Number of Epochs	Initial Learning Rate
Lead Red	h	46	332	0.0550
	L	28	281	0.0539
	C	34	201	0.0206
Lithargite	h	22	218	0.0121
	L	39	163	0.0186
	C	46	350	0.0858
Rouge	h	31	234	0.0482
	L	25	94	0.0211
	C	19	136	0.0082
Cinnabar	h	50	62	0.0586
	L	40	340	0.0107
	C	21	187	0.0129
Azurite	h	27	124	0.0192
	L	47	232	0.0058
	C	41	229	0.0093
Malachite	h	34	57	0.0366
	L	31	350	0.0190
	C	20	310	0.0114

4.2. Comparative Analysis of Color Prediction Based on the GWOAD-LSTM Model

In our study, optically simulated aging experiments were conducted on six pigments: lead red, lithargite, rouge, cinnabar, azurite, and malachite. The hue (h), lightness (L), and chroma (C) were predicted for each pigment. Table 3 presents the training accuracy of the BPNN, LSTM, GWO-LSTM, and GWOAD-LSTM models and contains the results of RMSE, MAE, and MAPE for the hue (h). Figure 10 shows the results of the comparison between the six pigments' predicted hues.

Table 3. RMSE, MAE, and MAPE errors for the prediction of hue (h) in six pigments.

Pigment Type	Evaluation Standards	Train Set			Test Set		
		RMSE	MAE	MAPE (%)	RMSE	MAE	MAPE (%)
Lead Red (h)	BPNN	0.1991	0.1193	0.2472	0.7156	0.6872	1.4880
	LSTM	0.2000	0.1616	0.3395	0.2680	0.2189	0.4761
	GWO-LSTM	0.2040	0.1643	0.3453	0.4119	0.3216	0.6988
	Proposed	0.1509	0.1207	0.2539	0.1841	0.1490	0.3228
Lithargite (h)	BPNN	0.3095	0.2258	0.3115	0.4443	0.3908	0.5401
	LSTM	0.2613	0.2025	0.2789	0.5261	0.4543	0.6282
	GWO-LSTM	0.2437	0.1881	0.2593	0.4134	0.3412	0.4733
	Proposed	0.2114	0.1606	0.2214	0.4073	0.3381	0.4688
Rouge (h)	BPNN	4.2246	1.8991	26.3730	5.8673	4.9861	38.7220
	LSTM	4.0463	1.8421	21.8229	3.7508	2.5750	20.9684
	GWO-LSTM	2.3363	0.9389	12.0732	2.0961	1.5238	11.2220
	Proposed	1.6224	0.6875	8.4318	1.6826	1.2668	9.0555
Cinnabar (h)	BPNN	0.4821	0.3703	1.1389	1.0630	0.7566	2.2167
	LSTM	0.1968	0.1519	0.4708	0.6109	0.4746	1.3998
	GWO-LSTM	0.1941	0.1552	0.4789	0.3749	0.3041	0.8908
	Proposed	0.1921	0.1484	0.4568	0.3428	0.2691	0.7929
Azurite (h)	BPNN	0.1836	0.1472	0.0519	0.2758	0.2180	0.0768
	LSTM	0.1764	0.1462	0.0515	0.4151	0.3690	0.1300
	GWO-LSTM	0.1617	0.1338	0.0471	0.3462	0.3082	0.1086
	Proposed	0.1083	0.0881	0.0310	0.1702	0.1363	0.0481
Malachite (h)	BPNN	0.8806	0.5897	0.3506	0.9628	0.9229	0.5360
	LSTM	0.3097	0.2534	0.1537	0.5835	0.5011	0.2911
	GWO-LSTM	0.3169	0.2601	0.1574	0.8252	0.7427	0.4317
	Proposed	0.2287	0.1893	0.1146	0.2022	0.1660	0.0963

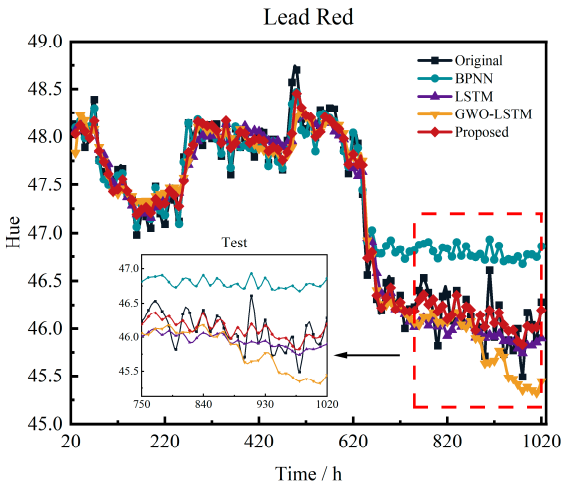

(**a**)

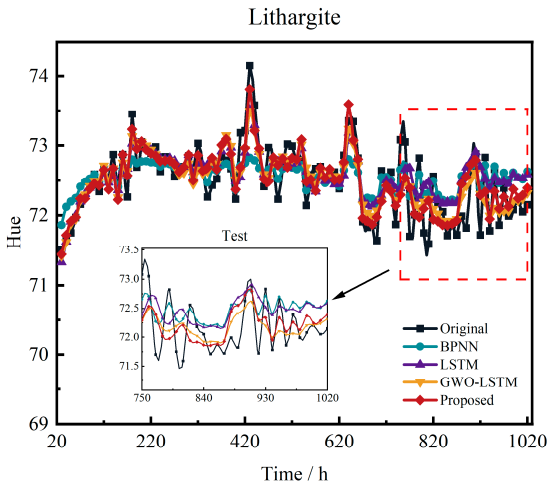

(**b**)

Figure 10. *Cont.*

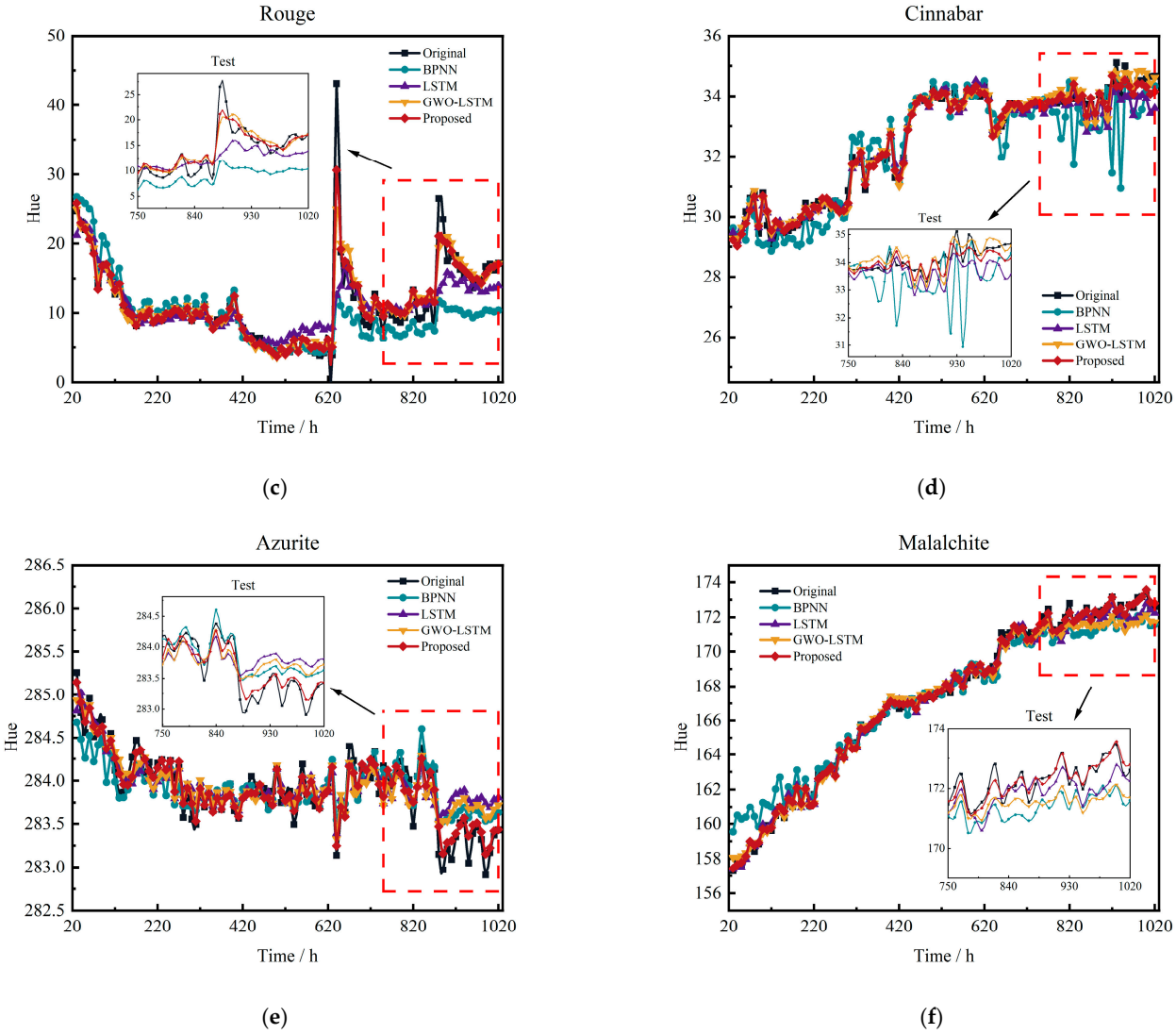

Figure 10. Comparison of the six pigments predicted Hue (h). Lead red (**a**), lighargite (**b**), rouge (**c**), cinnabar (**d**), azurite (**e**), and malalchite (**f**), respectively. (The subfigure shows the prediction results for the test set from 750 h to 1020 h).

From the graphs, for the hue (h) of six pigments, the BPNN model achieved an average RMSE of 1.0466, MAE of 0.5586, and MAPE of 4.7455%. The LSTM model achieved an average RMSE of 0.8651, MAE of 0.4596, and MAPE of 3.8529%. The GWO-LSTM model achieved an average RMSE of 0.5761, MAE of 0.3067, and MAPE of 2.2265%. The GWOAD-LSTM model demonstrated the best performance, with an average RMSE of 0.4190, MAE of 0.2324, and MAPE of 1.5849%. Our proposed optimized GWOAD-LSTM model had a higher accuracy of the training set than the other models. The RMSE decreased by 59.97%, 51.57%, and 27.27% on average; the MAE decreased by 58.40%, 49.43%, and 20.25% on average; and the MAPE decreased by 66.60%, 58.86%, and 28.82% on average compared with those from the BPNN, LSTM, and GWO-LSTM models, respectively. Thus, the GWOAD-LSTM model was better than the BPNN, LSTM, and GWO-LSTM models in terms of the accuracy for capturing the training samples with respect to the hue (h) when multiple data were processed.

Based on the test set in the prediction of hue (h), the BPNN model achieved an average RMSE of 1.5548, MAE of 1.3269, and MAPE of 7.2633%. The LSTM model achieved an average RMSE of 0.9749, MAE of 0.7655, and MAPE of 3.9823% for the same prediction task. The GWO-LSTM model achieved an average RMSE of 0.7446, MAE of 0.5903, and MAPE of

2.3042%. Our proposed optimized GWO-LSTM model achieved an average RMSE of 0.4982, MAE of 0.3876, and MAPE of 1.7974%. Our proposed optimized GWOAD-LSTM model had a higher prediction accuracy than the other models. The values decreased by 67.96%, 48.90%, and 33.09% on average for RMSE; by 70.79% 49.37%, and 34.34% on average for MAE; and by 75.25%, 54.87%, and 21.99% on average for MAPE compared with those from the BPNN, LSTM, and GWO-LSTM models, respectively. As a result, GWOAD-LSTM's prediction accuracy of the hue h was closer to the real value than the BPNN model, LSTM model, and GWO-LSTM model.

Based on the above, the GWOAD-LSTM model outperformed the BPNN, LSTM, and GWO-LSTM models in terms of data capture and prediction accuracy for the hue (h) prediction of the six pigments. This superiority was particularly evident in the prediction for the rouge and cinnabar pigments.

Table 4 shows the RMSE, MAE, and MAPE errors for the prediction of lightness (L) for the six pigments using the BPNN, LSTM, GWO-LSTM, and GWOAD-LSTM models; Figure 11 shows the comparison of the predicted lightness (L) for the six pigments. From the graphs, the GWOAD-LSTM model decreased the mean values of RMSE by 69.15%, 58.89%, and 18.78%; MAE by 64.09%, 58.38%, and 19.66%; and MAPE by 69.97%, 59.37%, and 21.01%, respectively, compared with those from the BPNN, LSTM, and GWO-LSTM models. The time series training accuracy of our proposed GWOAD-LSTM model was higher than those of the BPNN, LSTM, and GWO-LSTM models in terms of brightness L.

Table 4. RMSE, MAE, and MAPE errors for the prediction of lightness (L) in six pigments.

Pigment Type	Evaluation Standards	Train Set			Test Set		
		RMSE	MAE	MAPE (%)	RMSE	MAE	MAPE (%)
Lead Red (L)	BPNN	0.1787	0.1521	0.2513	0.3665	0.3473	0.5973
	LSTM	0.1897	0.1363	0.2247	0.7588	0.6653	1.1468
	GWO-LSTM	0.1479	0.1080	0.1791	0.1274	0.1084	0.1869
	Proposed	0.0797	0.0665	0.1099	0.0644	0.0546	0.0941
Lithargite (L)	BPNN	0.5946	0.4281	0.6877	1.0103	0.9705	1.6723
	LSTM	0.2875	0.2230	0.3645	0.2567	0.2090	0.3597
	GWO-LSTM	0.1904	0.1546	0.2537	0.1403	0.1219	0.2111
	Proposed	0.1763	0.1467	0.2424	0.1292	0.1037	0.1796
Rouge (L)	BPNN	1.2063	0.9603	1.5853	0.7502	0.5885	0.8440
	LSTM	1.1094	0.9044	1.5318	1.6937	1.4032	2.0342
	GWO-LSTM	0.4153	0.3547	0.5917	0.5738	0.4832	0.6936
	Proposed	0.4211	0.3299	0.5453	0.5305	0.4383	0.6195
Cinnabar (L)	BPNN	0.1837	0.1577	0.3263	0.3330	0.3084	0.6324
	LSTM	0.2394	0.1766	0.3642	0.3828	0.3033	0.6190
	GWO-LSTM	0.0876	0.0667	0.1378	0.1716	0.1319	0.2691
	Proposed	0.0676	0.0550	0.1132	0.1631	0.1135	0.2302
Azurite (L)	BPNN	0.2534	0.2032	0.5225	0.6198	0.5192	1.3131
	LSTM	0.1942	0.1521	0.3915	0.6516	0.5347	1.3677
	GWO-LSTM	0.0976	0.0721	0.1870	0.2516	0.1973	0.5079
	Proposed	0.0621	0.0491	0.1264	0.1244	0.1021	0.2549
Malachite (L)	BPNN	0.5108	0.4555	0.8558	0.7436	0.7080	1.3025
	LSTM	0.1763	0.1332	0.2499	0.2660	0.2160	0.3980
	GWO-LSTM	0.1731	0.1380	0.2586	0.2175	0.1605	0.2968
	Proposed	0.0960	0.0708	0.1329	0.1524	0.1222	0.2252

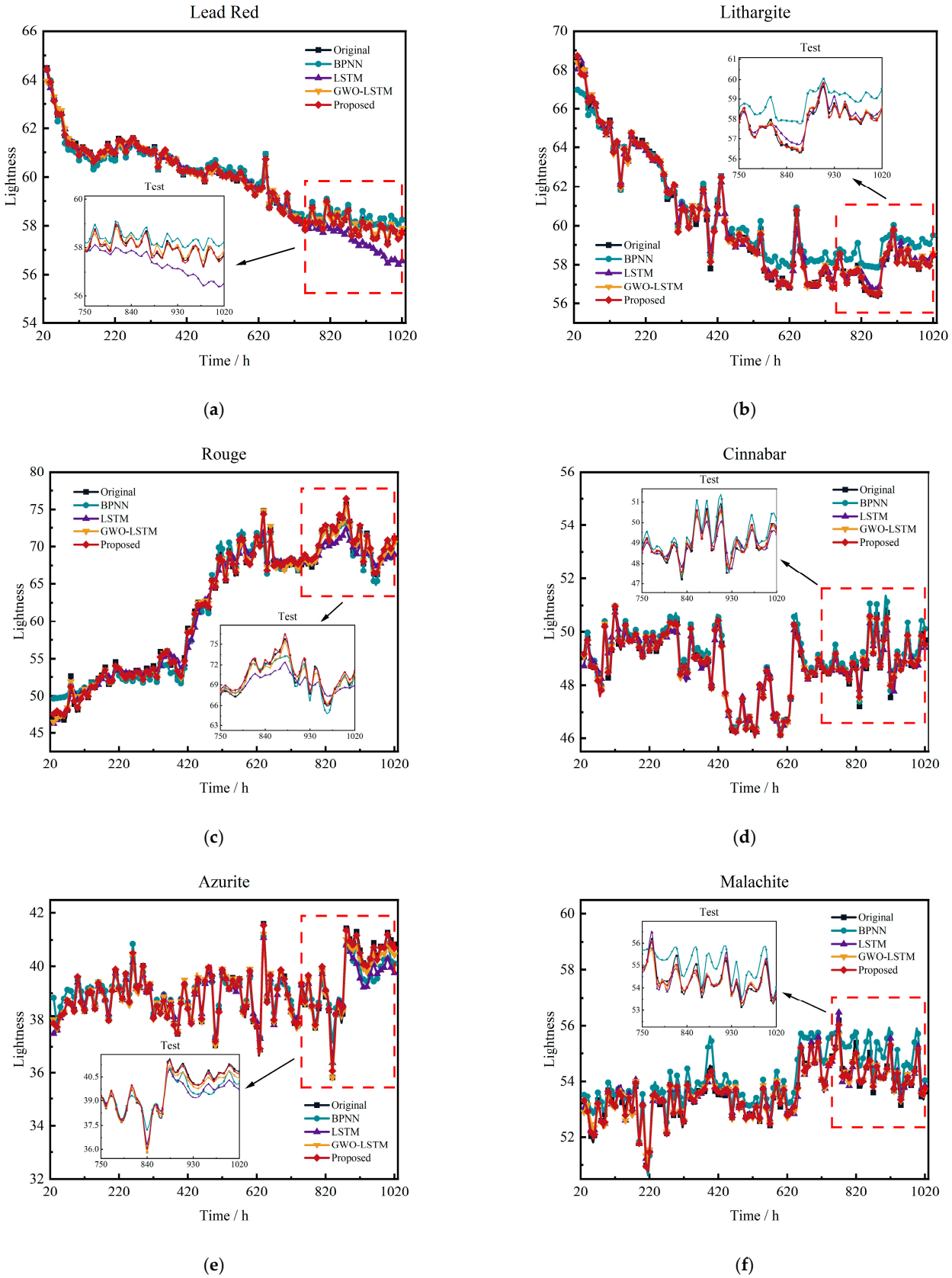

Figure 11. Comparison of the six pigments predicted lightness (L). Lead red (**a**), lighargite (**b**), rouge (**c**), cinnabar (**d**), azurite (**e**), and malalchite (**f**), respectively. (The subfigure shows the prediction results for the test set from 750 h to 1020 h).

In terms of the prediction accuracy of L, from the test set in the table, it can be seen that our proposed optimized GWOAD-LSTM model had a higher prediction accuracy than the other models. The values decreased by 67.84%, 69.34%, and 17.04% on average for RMSE; by 72.86%, 71.96%, and 15.70% on average for MAE; and by 74.79%, 72.93%, and 29.25% on average for MAPE, when compared with those from the BPNN, LSTM, and GWO-LSTM models, respectively. As a result, the prediction accuracy in the lightness L was closer to the true value than the former three models.

In summary, our proposed GWOAD-LSTM model showed greater advantages in the training and prediction of two pigments, rouge (L) and azurite (L). Overall, in terms of the training and prediction accuracy for the lightness (L) of all six pigments, our GWOAD-LSTM model outperformed the BPNN, LSTM, and GWO-LSTM models.

Table 5 shows the RMSE, MAE, and MAPE results of the six pigments for predicting chroma C. Figure 12 shows the comparison results of the six pigments for predicting C. As a result, the average RMSE of our proposed GWOAD-LSTM model was 52.34%, 40.22%, and 8.80% lower in the training set compared with those from the BPNN, LSTM, and GWO-LSTM models, respectively; the average MAE was 52.75%, 39.17%, and 9.28% lower, respectively; and the average MAPE was 46.45%, 34.99%, and 8.82% lower, respectively. In summary, the GWOAD-LSTM model had higher accuracy in training data capture.

Table 5. RMSE, MAE, and MAPE errors for the prediction of chroma (C) in six pigments.

Pigment Type	Evaluation Standards	Train Set			Test Set		
		RMSE	MAE	MAPE (%)	RMSE	MAE	MAPE (%)
Lead Red (C)	BPNN	0.4104	0.3518	0.5240	1.8323	1.6705	2.7773
	LSTM	0.4102	0.2931	0.4229	0.6732	0.5968	1.0074
	GWO-LSTM	0.3269	0.2478	0.3590	0.2964	0.2495	0.4184
	Proposed	0.2907	0.2208	0.3174	0.2327	0.1924	0.3232
Lithargite (C)	BPNN	0.3150	0.2121	0.8663	0.6359	0.5738	2.4161
	LSTM	0.4087	0.3228	1.3215	0.6834	0.5656	2.3675
	GWO-LSTM	0.2772	0.2274	0.9248	0.3743	0.3337	1.4093
	Proposed	0.2625	0.2037	0.8291	0.3084	0.2572	1.0884
Rouge (C)	BPNN	1.9875	1.2023	3.2957	3.3055	2.4920	9.9055
	LSTM	1.2415	0.9232	2.2448	3.2884	2.7364	9.9396
	GWO-LSTM	1.1530	0.8453	2.0764	2.5427	2.1453	8.0221
	Proposed	1.0347	0.7717	1.9016	2.3962	2.0374	7.6108
Cinnabar (C)	BPNN	0.3235	0.2612	0.6468	0.9354	0.9035	2.3552
	LSTM	0.3592	0.2752	0.6833	0.5652	0.4118	1.0678
	GWO-LSTM	0.2392	0.1835	0.4555	0.3636	0.2705	0.7038
	Proposed	0.1106	0.0877	0.2193	0.3315	0.2234	0.5778
Azurite (C)	BPNN	0.1867	0.1284	0.2548	0.4011	0.3328	0.6700
	LSTM	0.3848	0.3036	0.5999	0.5691	0.4202	0.8426
	GWO-LSTM	0.1235	0.0922	0.1823	0.2939	0.2243	0.4515
	Proposed	0.1109	0.0897	0.1774	0.2551	0.1998	0.4018
Malachite (C)	BPNN	0.3366	0.2202	0.5025	0.7800	0.5610	1.3338
	LSTM	0.4273	0.2866	0.6576	0.5106	0.3426	0.8023
	GWO-LSTM	0.1594	0.1157	0.2619	0.2524	0.1784	0.4213
	Proposed	0.1320	0.1023	0.2315	0.2362	0.1763	0.4172

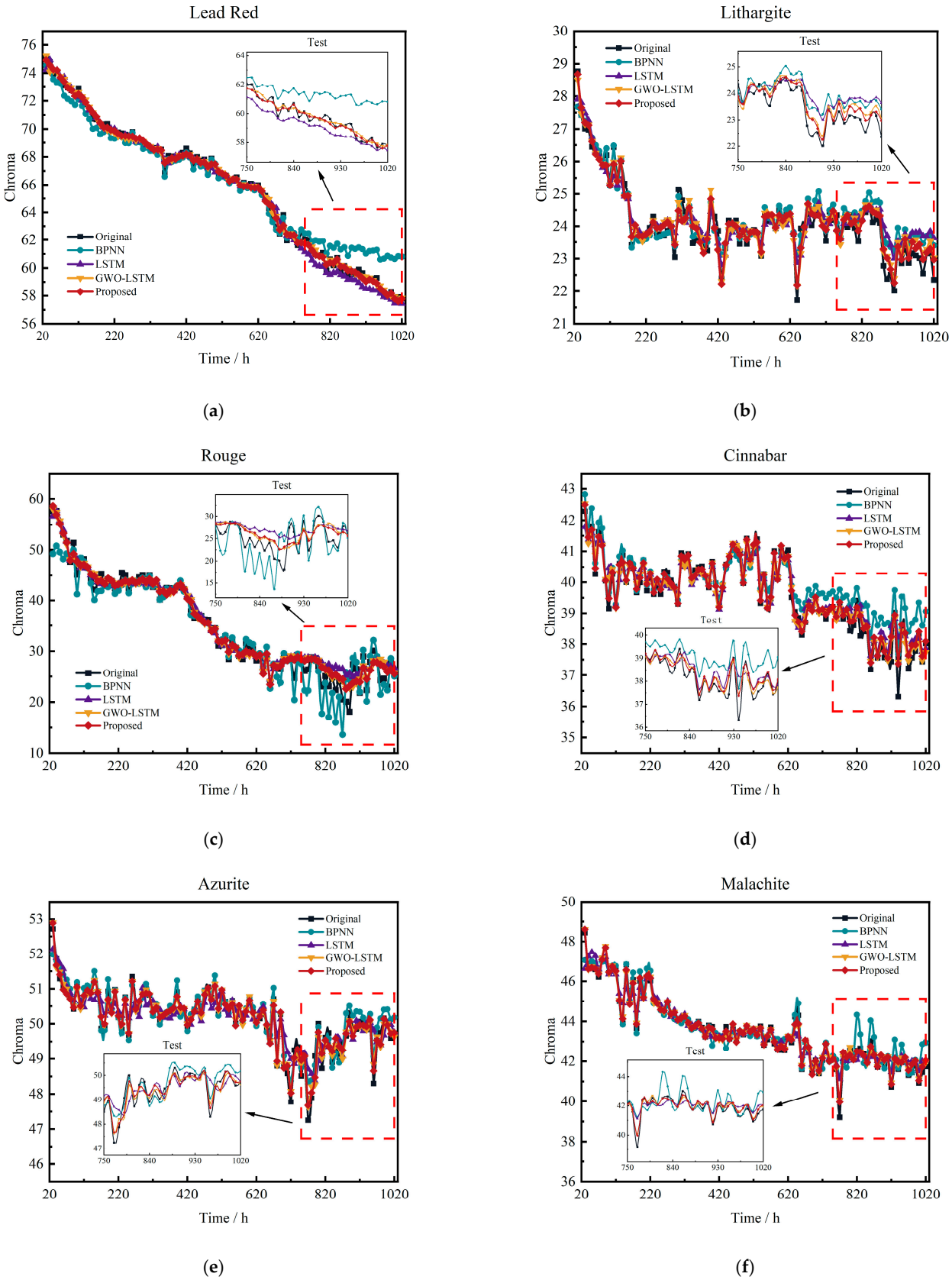

Figure 12. Comparison of the six pigments predicted chroma (C). Lead red (**a**), lighargite (**b**), rouge (**c**), cinnabar (**d**), azurite (**e**), and malalchite (**f**), respectively. (The subfigure shows the prediction results for the test set from 750 h to 1020 h).

Furthermore, in terms of data prediction, as a result, the GWOAD-LSTM model reduced the average RMSE by 69.96%, 39.02%, and 28.23%; the average MAE by 76.49%, 48.55%, and 28.23%; and the average MAPE by 68.84%, 47.60%, and 28.23% compared with those from the BPNN, LSTM, and GWO-LSTM models, respectively. Thus, the GWOAD-LSTM model was closer to the original data in terms of time series prediction.

Overall, when predicting the time series variation in chroma (C), our GWOAD-LSTM model outperformed the three previous models in terms of both training and prediction accuracy in the time series. This was particularly evident in accurately capturing data trends for the lead red, lithargite, and rouge pigments.

In summary, as shown in Figures 13 and 14, taking lead red as an example, the results predicted by the BPNN model and LSTM model for the six pigments' hLC optical change deviated from the actual results, and the prediction effect was gradually worsened as the time series increased; the GWO-LSTM model was slightly worse in the prediction accuracy and had the above phenomenon of gradually increasing prediction error; however, our proposed GWOAD-LSTM model had a larger overlap with the actual values in both training data and prediction data, the prediction effect was more ideal, and no phenomenon of the prediction effect becoming worse as the time series increased was observed. These were apparent advantages.

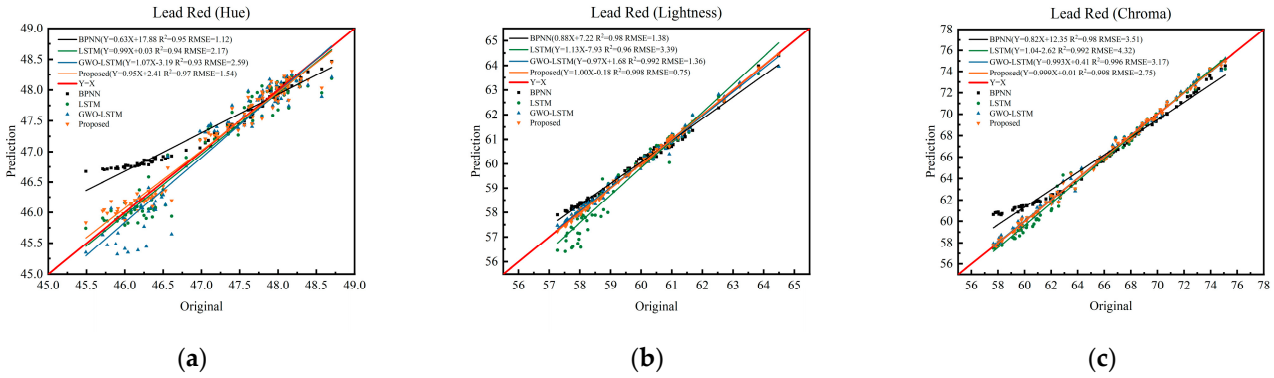

Figure 13. Scatter plot of prediction errors for the four models in predicting lead red. (Scatterplot of prediction error for lead red hue (**a**), lead red lightness (**b**), lead red chroma (**c**)).

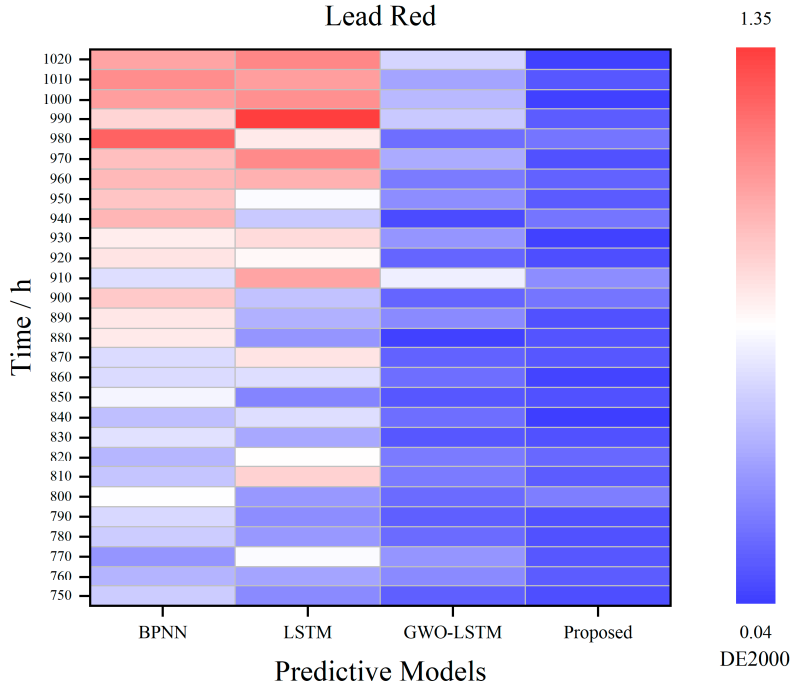

Figure 14. Comparison of color difference of the lead red test set.

According to the color blocks in Table 6, rouge had the largest variation. The different models had deviations in predicting the color of the color blocks. The predicted color of the BPNN model and the LSTM model had larger differences from the actual color. The GWO-LSTM model performed slightly better in prediction, but noticeable color differences were observed. In contrast, our proposed GWOAD-LSTM model demonstrated less color difference and better color reconstruction accuracy for rouge. Table 7 shows the average prediction results of the color gamut data for the six pigment test sets. The BPNN model and the LSTM model had lower color prediction accuracy, especially in the rouge color reconstruction with higher color differences. The GWO-LSTM model and GWOAD-LSTM model had good prediction results, among which our proposed GWOAD-LSTM model performed better in terms of color difference and has higher color reconstruction accuracy.

Table 6. Comparative visualization of rouge color blocks at different time sequences (outer ring: original color; inner ring: predicted color).

Model \ Time	130 h	420 h	810 h	1020 h
BPNN	ΔE = 1.66	ΔE = 2.30	ΔE = 3.21	ΔE = 2.09
LSTM	ΔE = 0.85	ΔE = 1.62	ΔE = 2.87	ΔE = 2.08
GWO-LSTM	ΔE = 0.44	ΔE = 0.51	ΔE = 2.11	ΔE = 0.52
Proposed	ΔE = 0.30	ΔE = 0.47	ΔE = 1.90	ΔE = 0.14

From the scatter plot analysis, the BPNN model had poor data capturing accuracy, the LSTM model exhibited weak data fitting amplitude, and the GWO-LSTM model showed low prediction accuracy in the peak. However, our GWOAD-LSTM model outperformed the other three models in terms of the above aspects. In particular, when applied to light-sensitive pigments, such as lead red, lithargite, and rouge, our GWOAD-LSTM model demonstrated superior prediction accuracy and generalization capability when compared to the BPNN, LSTM, and GWO-LSTM models. Additionally, the GWOAD-LSTM model slightly outperformed the other three models in the prediction accuracy for cinnabar, azurite, and malachite pigments, which had slighter hLC variations, where the color variations were relatively smaller. Therefore, our proposed GWOAD-LSTM model exhibited higher prediction accuracy and better generalization ability, particularly for pigments with larger color variations.

Table 7. Comparative visualization of average color blocks in the testing dataset (outer ring: original color; inner ring: predicted color).

Model / Pigment	Lead Red	Lithargite	Rouge	Cinnabar	Azurite	Malachite
BPNN	ΔE = 0.75	ΔE = 0.95	ΔE = 2.36	ΔE = 0.37	ΔE = 0.49	ΔE = 0.85
LSTM	ΔE = 0.67	ΔE = 0.44	ΔE = 2.08	ΔE = 0.30	ΔE = 0.55	ΔE = 0.36
GWO-LSTM	ΔE = 0.27	ΔE = 0.26	ΔE = 1.33	ΔE = 0.16	ΔE = 0.27	ΔE = 0.39
Proposed	ΔE = 0.13	ΔE = 0.23	ΔE = 1.25	ΔE = 0.13	ΔE = 0.13	ΔE = 0.17

4.3. Fade Analysis of the Pigment Color Blocks

① Lead Red: In the simulated aging fading, from Figures 10a, 11a, and 12a, the lightness (L) decreased from 64.5 to 57.3, the chroma (C) decreased from 75.1 to 57.8, and the hue (h) decreased during 20–250 h, increased during 250–370 h, and gradually decreased from 570 h. This analysis shows the following: As shown in Figure 7, the experimental light source did not show a spectral response in the longer wavelength range; its spectral response was mainly located in the 290–450 nm shorter wavelength range, which had a higher spectrum amplitude energy and was more easily excited. Wavelengths primarily in the range of 610–700 nm corresponded to lead red excitation; lead read is mainly composed of Pb_3O_4. Under long-term constant temperature and humidity conditions, high-energy blue-green light was absorbed to generate PbO_2, resulting in a decrease in lightness and chroma. Additionally, an overall yellowing and darkening occurred in the gelatin due to its absorption of high-energy spectra. However, the increase in hue between 250 and 370 h could be attributed to the decomposition of gelatin resulting from the absorption of a large amount of high-energy blue-green light. After 570 h, an overall shift toward a dark red hue occurred.

② Lithargite: In the simulated aging fading, as can be observed from Figure 11b, a nearly linear decrease in lightness (L) with a magnitude of 10 was observed. Lithargite underwent a transformation from PbO to PbO_2 with formation of a small amount of $PbCO_3 \cdot Pb(OH)_2$ [7], resulting in an overall decrease in lightness. From Figures 10b and 12b, the hue (h) increased from 71.5 to 73 during 0–220 h, while the chroma (C) sharply decreased during the same period and exhibited a relatively slow decline after 220 h. A substantial amount of short-wavelength blue light was absorbed by both lithargite and gelatin during this period, as indicated by their significant reflectance in the wavelength range of 570–670 nm. As a result, the gelatin underwent decomposition, leading to a shift toward a blue-green hue in the overall chromaticity.

③ Rouge: Rouge is a commonly used natural pigment with unstable properties that is prone to fading under prolonged exposure [4]. As shown in Figure 11c, a significant increase in lightness (L) with a value of 25.1 was exhibited by rouge during 400–600 h under simulated sunlight irradiation, resulting in an overall phenomenon of whitening and fading. From Figures 10c and 12c, a downward trend followed by a slight upward trend was observed in the hue (h), with a decrease from 24.8 to 3.9 and then an increase to 17.2. The overall hue gradually shifted from deep red to bluish-red. The chroma (C) demonstrated a decreasing trend with a value of 22.3. The experimental light source used in this study had a low spectral response in the range of 600–700 nm, leading to the prolonged absorption of high-energy blue-green light. Due to this long-term absorption, the red longer wavelength spectrum absorption was low, resulting in the aging and decomposition of gelatin, fading of rouge, and an overall lighter color.

④ Cinnabar: Cinnabar is also in the red family, but it is relatively stable. Its main component is mercury sulfide, a hexagonal crystal system, and its crystals are plate-like or rhombic [7]. When heated, a transformation of the crystal structure to a cubic (isometric) crystal system with a sphalerite-type structure occurred, resulting in dimming of the lightness. Upon cooling, the original structure was restored. From Figures 10d and 12d, an increase in hue (h) from 29 to 34 was observed, while the chroma (C) decreased from 42.5 to 38. Some dark cinnabar was produced, and gelatin decomposition occurred; however, the overall degree of color change was not evident.

⑤ Azurite and malachite: Both pigments are derivatives of Cu ions, with the molecular formulas $Cu(OH)_2(CO_3)_2$ for azurite and $Cu_2CO_3(OH)_2$ for malachite. Azurite is a companion mineral that forms together with malachite, surrounding the inner malachite, and they have similar chemical compositions [21]. From Figure 10, the hue (h) of azurite insignificantly decreased with a value of 2.1, and the hue (h) of malachite increased to a value of 15.3. From Figure 11, the overall lightness of malachite and azurite was more stable and less affected by external influences. In Figure 12e,f, there was a slight decrease in chroma (C) for both azurite and malachite, with a decrease of 3 and 6.7, respectively. These pigments reflected more to the blue and green wavelengths. In addition, the experimental light source had low yellow and red content, resulting in lower energies of medium and long wavelengths. Thus, the overall color change in the cyan pigment was small after absorbing a large amount of low-energy radiation. However, the hue (h) of malachite tended to be closer to cyan under prolonged light irradiation. The shortwave radiation was absorbed more by the green pigment than by the cyan pigment, resulting in a relatively larger change in hue (h).

In summary, red and yellow pigments were prone to chemical reactions and physical structure changes due to prolonged light irradiation, resulting in much more complex color appearance changes and larger data fluctuations compared to the cyan pigments. Figure 15a shows the average color difference ΔE_{00} comparison of all models across the entire time series. In terms of overall color difference comparison, especially for light-sensitive pigments, the GWOAD-LSTM model had better fitting long-term trends and more accurate data capture compared to the BPNN, LSTM, and GWO-LSTM models. As shown in Figure 15b, the GWOAD-LSTM model had the smallest color difference and outperformed the previous three models in terms of color gamut prediction, indicating that our proposed model could effectively handle short-term data fluctuations and had higher prediction accuracy. At the same time, there were many factors, such as noise, in the original data, which caused the GWOAD-LSTM composite model to predict the effect of pigment fading with a slight error from the real value, but the overall prediction accuracy was better. Therefore, our proposed GWOAD-LSTM model was feasible in the field of practical pigment fading simulation prediction and rare painting restoration.

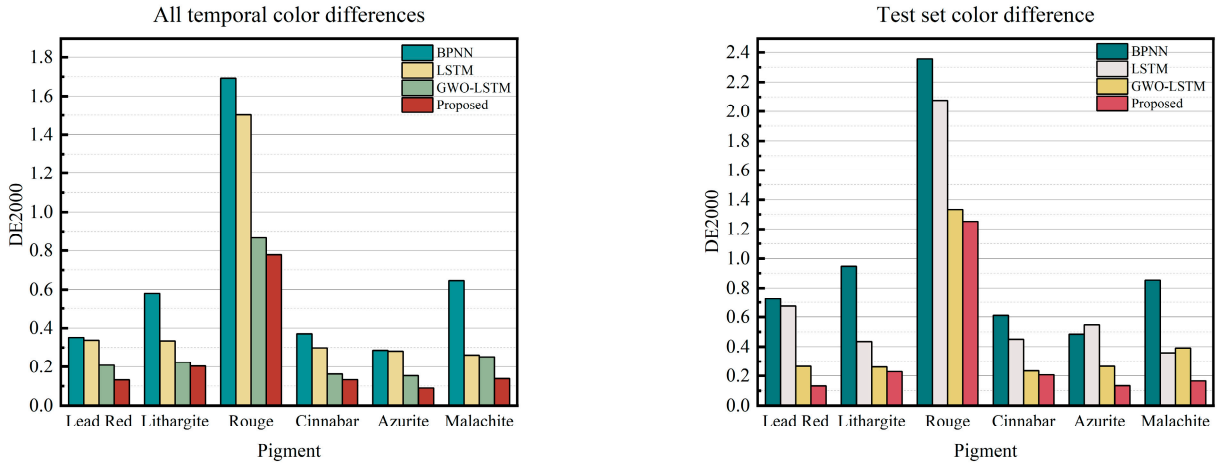

(**a**) (**b**)

Figure 15. Comparison of the average color difference for each model (**a**) and the average color difference for each model test set (**b**).

5. Conclusions

The new pigment chronological prediction model (GWOAD-LSTM) was proposed to improve the prediction accuracy of aging pigments. On the one hand, an improved multidimensional global search optimization algorithm (GWOAD) was proposed to diversify the gray wolf optimization search and enhance the robustness and exploration capacity of the GWOAD model. On the other hand, the optimized hyperparameters found by GWOAD were inputted in the LSTM model to achieve the time series prediction of the pigment color domain, avoiding the intricate hyperparameter selection in the LSTM model. Our proposed GWOAD-LSTM prediction model significantly outperformed the BPNN, LSTM, and GWO-LSTM models regarding the accuracy and generalization ability. In predicting red pigments, especially the light-sensitive rouge pigment, the original data drastically fluctuated. This potentially caused a slight shortage of peak capture and a weak lag phenomenon. However, regarding the overall prediction accuracy, including the capture by the training set of the original data and the prediction accuracy of the test set, the final error index was within the acceptable range. Thus, our proposed GWOAD-LSTM composite model was suitable for pigment simulation aging prediction and heritage conservation. In the future, improvements and extensions to the algorithm and model will be attempted in the raw noise processing area.

Author Contributions: Conceptualization, Z.L. and A.-R.Z.; methodology, A.-R.Z.; software, A.-R.Z.; experiment, A.-R.Z. and S.-L.L.; validation, Z.L., A.-R.Z. and S.-L.L.; formal analysis, A.-R.Z.; investigation, A.-R.Z.; resources, A.-R.Z.; data curation, A.-R.Z.; writing—original draft preparation, A.-R.Z.; writing—review and editing, Z.L., A.-R.Z. and S.-L.L.; visualization, A.-R.Z.; supervision, Z.L., A.-R.Z. and S.-L.L.; project administration, Z.L.; funding acquisition, Z.L. All authors have read and agreed to the published version of the manuscript.

Funding: This research was funded by the National Natural Science Foundation of China, grant number No. 61405104; Shandong Provincial Key research project on artistic science, grant number No. L2023Z04180033; and Humanities and Social Sciences Program of the Ministry of Education, grant number No.24YJAZH095.

Institutional Review Board Statement: Not applicable.

Informed Consent Statement: Not applicable.

Data Availability Statement: The original contributions presented in the study are included in the article; further inquiries can be directed to the corresponding authors.

Acknowledgments: We thank the anonymous reviewers for their valuable comments, which made this manuscript better.

Conflicts of Interest: The authors declare no conflicts of interest.

References

1. *The 13th Five-Year Plan for the Development of the National Cultural Relics Program*; National Cultural Heritage Administration: Beijing, China, 2017.
2. Chen, L. Research on the countermeasures for the development of museums in the era of "Internet +". *Jiangnan Forum* **2016**, 33–35. [CrossRef]
3. Berns, R.S. Digital color reconstructions of cultural heritage using color-managed imaging and small-aperture spectrophotometry. *Color Res. Appl.* **2019**, *44*, 531–546. [CrossRef]
4. Kirchner, E.; van der Lans, I.; Ligterink, F.; Geldof, M.; Ness Proano Gaibor, A.; Hendriks, E.; Janssens, K.; Delaney, J. Digitally reconstructing van Gogh's field with irises near Arles. Part 2: Pigment concentration maps. *Color Res. Appl.* **2018**, *43*, 158–176. [CrossRef]
5. Kirchner, E.; van der Lans, I.; Ligterink, F.; Geldof, M.; Megens, L.; Meedendorp, T.; Pilz, K.; Hendriks, E. Digitally reconstructing Van Gogh's Field with Irises near Arles part 3: Determining the original colors. *Color Res. Appl.* **2018**, *43*, 311–327. [CrossRef]
6. Bruder, R.; L'Hermite, D.; Semerok, A.; Salmon, L.; Detalle, V. Near-crater discoloration of white lead in wall paintings during laser induced breakdown spectroscopy analysis. *Spectrochim. Acta Part B At. Spectrosc.* **2007**, *62*, 1590–1596. [CrossRef]
7. Academy, D. *Dunhuang Research Anthology-Cave Conservation-Up*; Gansu Nationalities Publishing House: Lanzhou, China, 1993; pp. 111–117, 199–219.
8. Li, Z.; Fan, Z.; Sheng, F. New advances in the study of the discoloration of lead red cinnabar and earth red. *Dunhuang Res.* **1992**, 89–117+123–124+185.
9. Sheng, F.; Li, Z.; Fan, Z. Humidity is a major factor in the discoloration of lead red. *Dunhuang Res.* **1990**, 104–119+128–129.
10. Gong, M.; Xin, X.; Han, F.; Wang, L. Study on discoloration of Red Lead. *Relics Museolgy* **2009**, 479–486. [CrossRef]
11. Kai-Ging, Z.; Rui, D. Evaluation Method for Damage Degree of Light Sources Used to Lighting Colorful Cultural Relics Based on Spectrum Analysis. *Spectrosc. Spectr. Anal.* **2021**, *41*, 1886–1890.
12. Schmidhuber, J.; Hochreiter, S. Long short-term memory. *Neural Comput.* **1997**, *9*, 1735–1780.
13. Mirjalili, S.; Mirjalili, S.M.; Lewis, A. Grey wolf optimizer. *Adv. Eng. Softw.* **2014**, *69*, 46–61. [CrossRef]
14. Pan, J.; Jing, B.; Jiao, X.; Wang, S. Analysis and application of grey wolf optimizer-long short-term memory. *IEEE Access* **2020**, *8*, 121460–121468. [CrossRef]
15. Luo, Q.; Zhang, S.; Li, Z.; Zhou, Y. A novel complex-valued encoding grey wolf optimization algorithm. *Algorithms* **2015**, *9*, 4. [CrossRef]
16. Long, W.; Liang, X.; Cai, S.; Jiao, J.; Zhang, W. A modified augmented Lagrangian with improved grey wolf optimization to constrained optimization problems. *Neural Comput. Appl.* **2017**, *28*, 421–438. [CrossRef]
17. Wolpert, D.H.; Macready, W.G. No free lunch theorems for optimization. *IEEE Trans. Evol. Comput.* **1997**, *1*, 67–82. [CrossRef]
18. Zhang, X.; Wang, X. Comprehensive review of grey wolf optimization algorithm. *Comput. Sci.* **2019**, *46*, 30–38.
19. Wan, X.; Liang, J.; Sun, Z.; Li, C.; Guan, J.; Yu, Z.; Liu, Q.; Wang, Q. Dunhuang Frescoes' Color Cards and Their Production Methods. China Patent CN201610338411, 19 May 2016.
20. Liang, J.; Wan, X. Non-destructive pigment identification method of ancient murals based on visible spectrum. *Spectrosc. Spectr. Anal.* **2017**, *37*, 2519–2526.
21. Wang, X.; Yu, L. *Handbook of Mineral Colors: The Study and Expression of Mineral Pigments for Painting*; People's Fine Arts Publishing House: Beijing, China, 2008.

Disclaimer/Publisher's Note: The statements, opinions and data contained in all publications are solely those of the individual author(s) and contributor(s) and not of MDPI and/or the editor(s). MDPI and/or the editor(s) disclaim responsibility for any injury to people or property resulting from any ideas, methods, instructions or products referred to in the content.